Stability analysis of two-phase buoyancy-driven flow in the presence of a capillary transition zone

Hamid Emami Meybodi and Hassan Hassanzadeh*
Department of Chemical & Petroleum Engineering, Schulich School of Engineering, University of Calgary, Calgary, Alberta, Canada T2N 1N4
(Received 3 November 2012; published 13 March 2013)

Natural convection that results from the dissolution of a diffusive species into a fluid saturated porous layer in the presence of a capillary transition zone is an important phenomenon in geological flows. The prediction of the onset of convection has remained elusive under the theory of gravitationally unstable multiphase flow in porous media. The present study offers a paradigm for the stability of two-phase buoyancy-driven flow in the presence of the capillary transition zone in a saturated porous medium, which allows for a quantitative description of the onset of natural convection. The analysis, which is based on the quasi-steady-state approximation, stresses the critical role of the capillary transition zone and the upward crossflow between the diffusive boundary layer and the capillary transition zone in the stability of the system, as well as in the transient growth of perturbations. We show that the instability problem can be characterized by capillary-dominant and buoyancy-dominant regimes with a transition in between. In the capillary-dominant regime, capillarity has a strong role in destabilizing the diffusive boundary layer. While in the buoyancy-dominant regime, the capillary transition zone is small enough that it can be ignored and the buoyancy force is the sole cause of the instability. Furthermore, our analysis shows that the capillary transition zone can potentially accelerate the evolution of the natural convection over 6 times faster than the buoyancy-dominant regime. Finally, the nonlinear dynamics of the system is studied using direct numerical simulations. The nonlinear simulations confirm the predictions from the linear stability analysis.

DOI: 10.1103/PhysRevE.87.033009 PACS number(s): 47.56.+r, 47.20.−k, 47.55.−t, 47.51.+a

I. INTRODUCTION

The buoyancy-driven convection of a gravitational unstable diffusive boundary layer is a simple example of a physical system for the study of nonlinear fingering dynamics and pattern formation in multiphase flow through porous media. Rather than a diffusive boundary layer, the flow may become gravitationally unstable under some circumstances, and the evolution of instabilities forms the fingers of a dense fluid penetrating into a light fluid.

Buoyancy-driven flows in porous media have been extensively investigated [1–5], since the pioneering work of Horton and Rogers [6] and Lapwood [7], mainly due to the phenomenon's vast applications in various scientific and engineering disciplines. Intense experimental and theoretical works on the mixing induced by buoyancy-driven flows were reported in the 1970s [8], which were followed by numerous stability analyses of the boundary layer in porous media [9]. Natural thermal convection has often been the focus of applications, such as porous insulation and geothermal systems [10,11].

Increasing interest has recently been reported in the unsteady boundary layers, due to solute diffusion in the subsurface in the underground transport of pollutants and saltwater intrusion in coastal aquifers [12] and carbon dioxide (CO_2) sequestration in deep saline aquifers [13–15]. In these examples of solutal convection, the diffusion of a species into the resident fluid creates a diffusive boundary layer, which grows with time. As the mixed fluid density is greater than the resident fluid, the diffusive boundary layer may become unstable and set off natural convection. When convection begins, the dissolved substance is carried downwards. Such convective mixing reduces the time scale of mixing, while increasing the length at which a solute can penetrate deeply into the subsurface.

In most cases, it is assumed that the initial transport process is fast compared with the evolution of the boundary layer, which results in an instant rise in the concentration within the domain of interest. In some cases, such as the dissolution of CO_2 in deep saline aquifers, there is the additional complication of a two-phase region at the top boundary, which is usually simplified into a boundary condition of a constant solute concentration for a single-phase system [16].

Despite overwhelming experimental and theoretical evidence, the role of capillarity in the two-phase buoyancy-driven flow in porous media has remained elusive. As mentioned earlier, the majority of past investigations on the stability of convective flows in porous media are based on a single-phase flow region, where the top boundary is exposed to a constant concentration of the diffusing species. In the traditional approach, it is assumed that there is no flow across the top boundary and the dissolution process occurs purely in a single-phase region, which is the mixing region [17].

To assess the contribution of a capillary transition zone, Elenius *et al.* [18] considered a crossflow between the capillary transition zone and the diffusive boundary layer. Rather than implementing the traditional closed boundary for velocity at the top of domain, they assigned a homogeneous Neumann (second-type) boundary condition to consider the effect of the crossflow. The resulting stability condition showed that the crossflow has no significant effect on the selection of the critical mode. However, it exerts a destabilizing influence on the boundary layer, such that the onset of instabilities occurs much earlier, up to 5 times faster when the diffusive boundary layer is thin. To the best of the authors' knowledge, no previous studies have explicitly investigated the role of the capillary transition zone on the stability of a gravitational unstable

*hhassanz@ucalgary.ca

diffusive boundary layer underneath a capillary transition zone.

The stability of a steady or transient concentration or temperature base profiles under a variety of boundary conditions has been thoroughly investigated [19–29]. For instance, Riaz *et al*. [30] performed a linear stability analysis (LSA) based on the dominant mode of the self-similar diffusion operator and direct numerical simulations. They presented scaling relationships for the onset of convection with respect to the Rayleigh number, which is the ratio of the driving buoyancy forces to the dissipative effects of viscosity and diffusion.

Several methods have been used to characterize the stability of a time-dependent concentration or temperature profiles, including amplification theory [18,30–34], local Rayleigh number analysis [9,35], the energy method [25,32,36], and the quasi-steady-state approximation (QSSA) [28,31,37,38]. Onset times predicted by the energy method are such that the energy stability analysis yields an earlier time of onset than the amplification theory [32]. In addition, the energy methods give no information about the growth rate and wave number of the most detrimental disturbances. For *steady-state* convection, the amplification theory leads to an algebraic eigenvalue problem [22,39], whereas the boundary layer remains time dependent. For such stability problems, QSSA has been widely used and is a common approach using the frozen-time concept.

The present study aims at the development of an LSA of a gravitationally unstable diffusive boundary layer in the presence of a capillary transition zone. In particular, the critical role of the capillary transition zone and the role of the relative permeability on the onset of instability are examined. In order to analyze the long-term evolution of the instability predicted by the LSA, a set of two-phase direct nonlinear numerical simulations has been carried out. The results presented in this study provide a better understanding of the effects of the capillary transition zone on the stability of the diffusive boundary layer.

The paper is organized as follows. Section II presents the mathematical formulations that include the governing equations. The base state solutions for the saturation and concentration fields, around which the model is linearized, are also shown in this section. Section III introduces the linearized problem and its discretization, and the results of the stability analysis are also presented. The results of nonlinear simulations are given in Sec. IV; and, finally, the main conclusions of the present study are summarized in Sec. V.

II. MATHEMATICAL FORMULATION

A two-dimensional (2D) fluid-saturated porous layer with a capillary transition zone and a gas cap on top where the gravity points downward in the positive z direction is considered, as shown in Fig. 1. The porous layer is modeled as a homogeneous and isotropic medium. Initially, the gas cap is saturated with the nonwetting phase and residual wetting phase ($s_w = s_{wr}$), while the underlying domain is fully saturated with the wetting phase ($s_w = 1$). Above the wetting phase zone, the wetting phase saturation decreases gradually upward, until it reaches a residual value, s_{wr}, which forms a transition zone. In other words, due to the capillary effect, a transition zone is expected to form between the nonwetting and wetting regions. Since the nonwetting phase (gas) is less dense than the wetting phase (water), the two-phase system remains gravitationally stable.

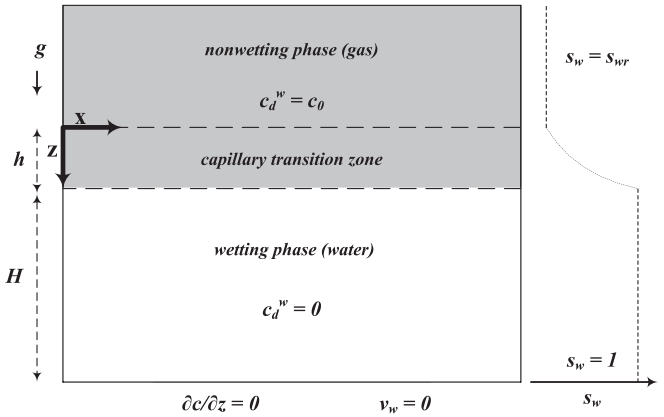

FIG. 1. Schematic presentation of the initial state of the two-phase system in a simple geometry. The porous layer is saturated with the wetting phase at the bottom. The saturated zone is overlaid by a capillary transition zone where the wetting phase saturation decreases gradually upward until it reaches a residual saturation value. The gas component can diffuse from the unsaturated zone into the underlying wetting phase, resulting in a downward flux of gas.

The diffusion of gaseous species from the gas cap into the underlying water zone may, however, lead to a slight increase in water density [e.g., dissolution of sulphur dioxide (SO_2) and CO_2 in water], consequently resulting in a gravitationally unstable diffusive boundary layer that grows with time and can potentially create convective instabilities in the water-saturated zone and wetting phase mobile portion of the transition zone. Therefore, the capillary transition zone combined with the underlying wetting phase region is considered the domain of study for the investigation of the role of the transition zone on the onset of buoyancy-driven convection. Note that, in this paper, the interface refers to the initial state of the dividing horizon between the capillary transition zone and the diffusive boundary layer, as shown in Fig. 1.

In the following subsections, the mathematical formulations for the flow and transport of a two-phase and two-component system described above are presented.

A. Governing equations

The governing equations for the dynamics of Boussinesq flow for the two-phase system are given by the multiphase extension of Darcy's law [40,41]:

$$\mathbf{v}_w = -\frac{kk_{rw}}{\mu_w}(\nabla p_w - \rho_w g \nabla z), \tag{1}$$

$$\mathbf{v}_n = -\frac{kk_{rn}}{\mu_n}(\nabla p_n - \rho_n g \nabla z), \tag{2}$$

$$\phi\frac{\partial s_w}{\partial t} = -\nabla\cdot\mathbf{v}_w, \tag{3}$$

$$\phi\frac{\partial s_n}{\partial t} = \nabla\cdot\mathbf{v}_n, \tag{4}$$

$$\mathbf{v} = \mathbf{v}_w + \mathbf{v}_n, \tag{5}$$

$$\nabla \cdot \mathbf{v} = 0, \tag{6}$$

$$p_c = p_n - p_w, \tag{7}$$

$$s_w + s_n = 1, \tag{8}$$

where k is the absolute permeability; k_r is the relative permeability; μ is the viscosity; ρ is the density; g is the gravity acceleration; ϕ is the porosity; $\mathbf{v} = [u,v]$ and is the velocity vector, where u is the horizontal component of velocity and v is the vertical component of velocity; s is the saturation defined as the macroscopic quantity that describes the average volume fraction of one phase in a representative elementary volume normalized by porosity; and subscripts w and n refer to the wetting and the nonwetting phases, respectively.

The equation for the saturation of the wetting phase that holds capillary and gravity forces is obtained by combining Eqs. (1), (2) and (5)–(7) as

$$\nabla \cdot \left(\mathbf{v}_w \left(1 + \frac{k_{rn}}{k_{rw}} \frac{\mu_w}{\mu_n} \right) - \frac{k k_{rn}}{\mu_n} \left[\frac{dp_c}{ds_w} \nabla s_w + (\rho_w - \rho_n) g \nabla z \right] \right) = 0. \tag{9}$$

The two-phase convection-diffusion equation, which governs dissolution of the diffusive species c_d^w into the resident fluids (wetting phase), is written as [1]

$$\phi \frac{\partial}{\partial t} \left(s_w c_d^w \right) = -\nabla \cdot \left(\mathbf{v}_w c_d^w \right) + D\phi \nabla \cdot \left(s_w \nabla c_d^w \right), \tag{10}$$

where D is the molecular diffusion coefficient.

The density of the wetting phase ρ_w is specified as a linear function of concentration c_d^w:

$$\rho_w = \rho_{w0} \left(1 + \beta c_d^w \right), \tag{11}$$

where $\beta = \partial \rho_w / \rho_w \partial c_d^w$ and is considered constant and ρ_{w0} is the density of the wetting phase at $c_d^w = 0$.

The pressure can be eliminated using the stream function definition. Combining $u_w = -\partial \psi / \partial z$ and $v_w = \partial \psi / \partial x$ with Eqs. (1) and (11) gives the flow equation for the system under consideration,

$$\nabla^2 \psi = \frac{k k_{rw} g \rho_{w0} \beta}{\mu_w} \frac{\partial c_d^w}{\partial x}, \tag{12}$$

where ψ is the stream function.

B. Nondimensional equations

For analysis purposes, it is convenient to write governing equations in a dimensionless form. The model is nondimensionalized by selecting the domain depth H as the length scale and D/H^2 as the time scale. For simplicity, the origin of the space coordinate is transferred to the interface between the gas and the water. Accordingly, nondimensional space and time parameters can be expressed as

$$\eta = \frac{x}{H}, \quad \varsigma = \frac{z - h}{H}, \quad \tau = \frac{D}{H^2} t. \tag{13}$$

The nondimensional forms of capillary pressure, saturation, concentration, and stream function are defined as follows:

$$P_c = \frac{p_c}{\Delta \rho_{wn} g H}, \quad S = \frac{s_w - s_{wr}}{1 - s_{wr}}, \quad C = \frac{c_d^w}{c_0}, \quad \Psi = \frac{\psi}{D\varphi}, \tag{14}$$

where $\varphi = \phi(1 - s_{wr})$ is the effective porosity in the two-phase system, and $\Delta \rho_{wn} = \rho_w - \rho_n$ is the density difference between the wetting and nonwetting phases.

The system under consideration can be explored with the following nondimensional groups:

$$\mathrm{Ca} = \frac{H}{h} \text{ (Capillary number)}, \tag{15}$$

$$\mathrm{Ra} = \frac{k \Delta \rho_d^w g H}{D \varphi \mu_w} \text{ (Rayleigh number)}, \tag{16}$$

where $\Delta \rho_d^w = \rho_{w0} \beta c_0$ is the solutal density difference originated by dissolution of the diffusing species (gas) into the resident fluid (water) and h is the capillary rise, whose dependence on the system parameters is given by the Leverett scaling [42],

$$h \sim \frac{\gamma \cos \theta}{\Delta \rho_{nw} g \sqrt{k/\varphi}}, \tag{17}$$

where γ is the surface tension between the wetting and nonwetting phases and θ is the contact angle between the fluids interface and the rock surface, which quantifies the wettability of the rocks by the fluids [43].

Based on these definitions and the understanding of the space and time coordinates as their dimensionless counterparts, the nondimensional form of the governing equations for flow, wetting phase saturation, and transport can be expressed as

$$\nabla^2 \Psi = k_{rw} \mathrm{Ra} \frac{\partial C}{\partial \eta}, \tag{18}$$

$$\frac{\partial S}{\partial \tau} = \frac{k_{rw}}{\lambda} \left(\frac{\partial \Psi}{\partial \eta} \left(\frac{\lambda}{k_{rw}} \right)' \frac{\partial S}{\partial \varsigma} - \mathrm{Ra} G \left[(k_{rn} J') \nabla^2 S + (k_{rn} J')' \left(\frac{\partial S}{\partial \varsigma} \right)^2 + k_{rn}' \frac{\partial S}{\partial \varsigma} \right] \right), \tag{19}$$

$$S \frac{\partial C}{\partial \tau} = \frac{\partial \Psi}{\partial \varsigma} \frac{\partial C}{\partial \eta} - \frac{\partial \Psi}{\partial \eta} \frac{\partial C}{\partial \varsigma} + \nabla S \cdot \nabla C + S \nabla^2 C, \tag{20}$$

where $J(S) = \mathrm{Ca} P_c(S)$ is a dimensionless capillary pressure function, $G = k \Delta \rho_{nw} g / U \mu_w$ is the gravity number, $U = k \Delta \rho_d^w g / \mu_w$ is the buoyancy velocity, $\lambda = k_{rw} M + k_{rn}$ is the total mobility, $M = \mu_n / \mu_w$ is the viscosity ratio, and primes denote derivatives with respect to saturation S. These governing equations are subject to the following boundary conditions:

$$\Psi(\eta, \varsigma = -h/H, \tau) = 0, \quad \Psi(\eta, \varsigma = 1, \tau) = 0, \tag{21}$$

$$S(\eta, \varsigma = -h/H, \tau) = 0, \quad S(\eta, \varsigma = 1, \tau) = 1, \tag{22}$$

$$C(\eta, \varsigma = -h/H, \tau) = 1, \quad C(\eta, \varsigma = 1, \tau) = 0. \tag{23}$$

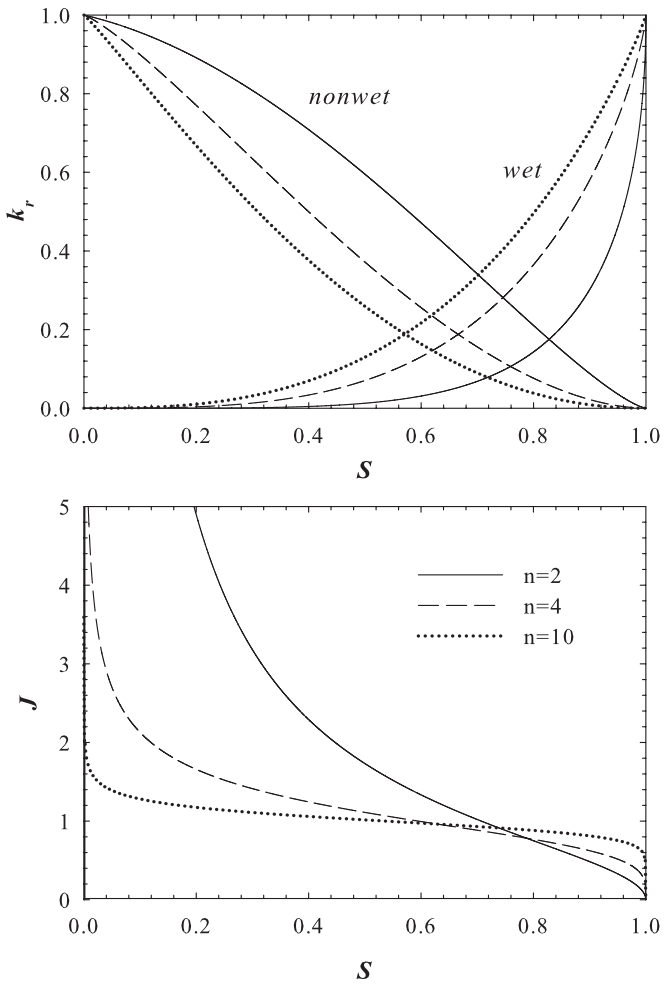

FIG. 2. Constitutive relations for relative permeabilities and capillary pressure as given by van Genuchten's model.

The functional forms of the relative permeabilities and capillary pressure constitutive relations are adopted from the van Genuchten-Mualem model [44,45],

$$k_{rn}(S) = (1-S)^{1/3}[1-S^{1/m}]^{2m}, \tag{24}$$

$$k_{rw}(S) = S^{1/2}[1-(1-S^{1/m})^{m}]^{2}, \tag{25}$$

$$J(S) = (S^{-1/m}-1)^{1/n}, \tag{26}$$

where $m = 1-1/n$ and n is the material parameter that depends on degree of sorting grains in the porous medium [44]. These functions are plotted in Fig. 2 for three different values of n.

C. Base-state solutions

The base state that results on dissolution of the diffusing species into the underlying water in a horizontal porous layer is examined. The base stream function Ψ_o that represents velocity is zero. Although a streamwise velocity does not exist, this term is used to describe the perturbation stream function component in the direction of acceleration due to gravity. The base saturation S_o is obtained based on capillary-gravity equilibrium using van Genuchten's capillary pressure constitutive relation [46],

$$S_o(\varsigma) = 1 + \mathbf{H}(-\varsigma)([1+(-\upsilon \mathrm{Ca}\varsigma)^n]^{-m} - 1), \tag{27}$$

where $\mathbf{H}(-\varsigma)$ is the Heaviside step function and υ is the matching parameter that forces the saturation of s_{wr} at the top boundary of the capillary transition zone, which should be assigned according to the value of n. Note that the saturation base state is time independent, since the saturation profile is caused by the equilibration of the capillary and gravity forces.

The base concentration C_o is the solution of Eq. (21) with $\partial/\partial\varsigma = \partial/\partial\eta = \partial^2/\partial\eta^2 = 0$, which admits the following streamwise one-dimensional (1D) solution [47]:

$$C_o(\varsigma,\tau) = 1 - 2\mathbf{H}(\varsigma)\sum_{l=1}^{\infty}\frac{1}{\alpha}\sin(\alpha\varsigma)\exp(-\alpha^2\tau), \tag{28}$$

where $\alpha = (2l-1)\pi/2$.

Note that the concentration base state is time dependent and that the penetration depth of the diffusive boundary layer $\delta(\tau)$, the depth over which C_o is nonzero, can be considered small compared to the depth of domain. For $\delta \sim \sqrt{4\tau} \ll 1$, the domain behaves as a semi-infinite medium in the z direction, i.e., $C(z\to\infty)\to 0$, and the base concentration can be expressed by [47]

$$C_o(\varsigma,\tau) = 1 - \mathbf{H}(\varsigma)\mathrm{erf}\left(\frac{\varsigma}{\sqrt{4\tau}}\right). \tag{29}$$

The objective of employing a semi-infinite domain is to achieve considerable improvement in accuracy at small times. For the original layer geometry in a finite domain, the parameter range over which the results are valid should obey $\delta \sim \sqrt{4\tau} \ll 1$. Note that the semi-infinite domain does not impose a new length scale on the problem under consideration. The penetration depth is time dependent, as is the Rayleigh number based on $\delta(\tau)$. A critical Rayleigh number is a function of the critical time at which the boundary layer becomes unstable, i.e., $\mathrm{Ra}_c = \mathrm{Ra}(\delta(\tau_c))$, and the length scale can be scaled out of calculations by specifying the time scale as a ratio of the diffusion coefficient to the square of the height, D/H^2. In this case, the critical time is the only criterion for the onset of instability.

III. LINEAR STABILITY ANALYSIS

A. Linearized equations

The interest of this study is the stability of the diffusive boundary layer in the presence of a capillary transition zone. In order to conduct an LSA, small disturbances of stream function $\hat{\Psi}$, saturation $\hat{S}$, and concentration $\hat{C}$ are introduced, and the equations are then linearized. In the semi-infinite domain, the perturbation equations are transformed in such a way that the eigenfunctions associated with the diffusion operator can be localized around the front of the base concentration. Therefore, a coordinate transformation of $\xi = \varsigma/\sqrt{4\tau}$ is applied on the perturbation equations. Since the base-state equations are independent of η, the perturbations decompose into Fourier components in the x direction. The perturbations are assumed

to be small in magnitude, therefore

$$\begin{Bmatrix} \Psi \\ S \\ C \end{Bmatrix}(\eta,\xi,\tau) = \begin{Bmatrix} \Psi_o \\ S_o \\ C_o \end{Bmatrix}(\eta,\xi) + \varepsilon \begin{Bmatrix} i\hat{\Psi} \\ \hat{S} \\ \hat{C} \end{Bmatrix}(\xi,\tau)\, e^{i\kappa\eta}, \tag{30}$$

where κ is the horizontal wave number, and its amplitude ε is assumed to be sufficiently small and the higher powers may be neglected.

Introducing the perturbed solutions in Eqs. (19)–(21) and retaining the terms that are the first order in ε, the evolution equations for the perturbations in the transformed coordinate are

$$\left(\frac{1}{4\tau}\frac{\partial^2}{\partial\xi^2} - \kappa^2\right)\hat{\Psi} - k_{rw}\mathrm{Ra}\kappa\hat{C} = 0, \tag{31}$$

$$\begin{aligned}\frac{\partial\hat{S}}{\partial\tau} = &-\frac{\kappa}{\sqrt{4\tau}}\frac{k_{rw}}{\lambda}\left(\frac{k_{rn}}{k_{rw}}\right)'\frac{\partial S_o}{\partial\xi}\hat{\Psi} - \frac{\mathrm{Ra}G}{4\tau}\left(\frac{k_{rw}}{\lambda}(k_{rn}J')\frac{\partial^2}{\partial\xi^2}\right.\\ &+\left[2\frac{k_{rw}}{\lambda}(k_{rn}J')'\frac{\partial S_o}{\partial\xi} + \sqrt{4\tau}\frac{k_{rw}}{\lambda}k'_{rn} - \frac{2\xi}{\mathrm{Ra}G}\right]\frac{\partial}{\partial\xi}\\ &+\left(\frac{k_{rw}}{\lambda}(k_{rn}J')\right)'\frac{\partial^2 S_o}{\partial\xi^2} + \left(\frac{k_{rw}}{\lambda}(k_{rn}J')'\right)'\left(\frac{\partial S_o}{\partial\xi}\right)^2\\ &+\sqrt{4\tau}\left(\frac{k_{rw}}{\lambda}k'_{rn}\right)'\frac{\partial S_o}{\partial\xi} - 4\tau\kappa^2\frac{k_{rw}}{\lambda}(k_{rn}J')\Big)\hat{S},\end{aligned} \tag{32}$$

$$\begin{aligned}S_o\frac{\partial\hat{C}}{\partial\tau} = &\frac{\kappa}{\sqrt{4\tau}}\frac{\partial C_o}{\partial\xi}\hat{\Psi} + \frac{1}{4\tau}\frac{\partial C_o}{\partial\xi}\frac{\partial\hat{S}}{\partial\xi}\\ &+\frac{1}{4\tau}\left(S_o\frac{\partial^2}{\partial\xi^2} + \left(2\xi S_o + \frac{\partial S_o}{\partial\xi}\right)\frac{\partial}{\partial\xi} - 4\tau\kappa^2 S_o\right)\hat{C},\end{aligned} \tag{33}$$

where the relative permeabilities and capillary pressure are decomposed using the first-order Taylor expansion $\{k_r, J\} = \{k_r, J\}(S_o) + \hat{S}\{k_r, J\}'$.

Moreover, the relative permeabilities and capillary terms and their derivatives in the perturbation equations should be evaluated according to the base states. It is important to note that the transformation of the coordinate from ς to ξ inserts the term $2\xi\partial/\partial\xi$ in both the saturation and transport equations.

B. Quasi-steady-state approximation and discretization

In the perturbation equations, the concentration base state is a function of both time τ and space ς. In order to solve the linearized equations numerically, the time dependence of the base state is eliminated using the QSSA [48]. This approximation assumes that the growth rate of perturbations is asymptotically faster than the evolution rate of the base state. As such, the concentration base state is frozen at a time τ_0, and the stability of this frozen profile is determined by expanding the disturbances in terms of Fourier components. Therefore, defining

$$\begin{Bmatrix} \hat{\Psi} \\ \hat{S} \\ \hat{C} \end{Bmatrix}(\xi,\tau) = \begin{Bmatrix} \Psi^* \\ S^* \\ C^* \end{Bmatrix}(\xi,\tau_0)\, e^{\sigma(\tau_0)\tau} \tag{34}$$

and substituting into Eqs. (31)–(33) gives

$$\left(\frac{1}{4\tau}\frac{\partial^2}{\partial\xi^2} - \kappa^2\right)\Psi^* - k_{rw}\mathrm{Ra}\kappa C^* = 0, \tag{35}$$

$$\begin{aligned}&-\frac{\kappa}{\sqrt{4\tau}}\frac{k_{rw}}{\lambda}\left(\frac{k_{rn}}{k_{rw}}\right)'\frac{\partial S_o}{\partial\xi}\Psi^* - \frac{\mathrm{Ra}G}{4\tau}\left(\frac{k_{rw}}{\lambda}(k_{rn}J')\frac{\partial^2}{\partial\xi^2}\right.\\ &+\left[2\frac{k_{rw}}{\lambda}(k_{rn}J')'\frac{\partial S_o}{\partial\xi} + \sqrt{4\tau}\frac{k_{rw}}{\lambda}k'_{rn} - \frac{2\xi}{\mathrm{Ra}G}\right]\frac{\partial}{\partial\xi}\\ &+\left(\frac{k_{rw}}{\lambda}(k_{rn}J')\right)'\frac{\partial^2 S_o}{\partial\xi^2} + \left(\frac{k_{rw}}{\lambda}(k_{rn}J')'\right)'\left(\frac{\partial S_o}{\partial\xi}\right)^2\\ &+\sqrt{4\tau}\left(\frac{k_{rw}}{\lambda}k'_{rn}\right)'\frac{\partial S_o}{\partial\xi} - 4\tau\kappa^2\frac{k_{rw}}{\lambda}(k_{rn}J')\Big)S^* - \sigma S^* = 0,\end{aligned} \tag{36}$$

$$\begin{aligned}&\frac{\kappa}{S_o\sqrt{4\tau}}\frac{\partial C_o}{\partial\xi}\Psi^* + \frac{1}{S_o 4\tau}\frac{\partial C_o}{\partial\xi}\frac{\partial S^*}{\partial\xi}\\ &+\frac{1}{4\tau}\left(\frac{\partial^2}{\partial\xi^2} + \left(2\xi + \frac{\partial S_o}{S_o\partial\xi}\right)\frac{\partial}{\partial\xi} - 4\tau\kappa^2\right)C^* - \sigma C^*,\end{aligned} \tag{37}$$

which are subject to the following boundary conditions:

$$\Psi^*(\xi = -h/H\sqrt{4\tau}) = 0, \quad \Psi^*(\xi = \infty) = 0, \tag{38}$$

$$S^*(\xi = -h/H\sqrt{4\tau}) = 0, \quad S^*(\xi = \infty) = 0, \tag{39}$$

$$C^*(\xi = -h/H\sqrt{4\tau}) = 0, \quad C^*(\xi = \infty) = 0, \tag{40}$$

where the variables that are defined by asterisks represent the perturbation eigenfunctions and σ is the quasistatic growth rate that appears as the eigenvalues in the problem.

The set of ordinary differential equations is discretized using a finite difference technique, which leads to an algebraic eigenvalue value problem. A finite difference method is convergent if the approximation solution approaches the exact solution as the sizes of the grids go to zero [49]. Therefore, a nonuniform geometric grid is employed, which is very fine in vicinity of the interface ($\varsigma = 0$), and the grid spacing increases logarithmically with the distance from the interface. This kind of discretization efficiently improves the accuracy, while decreasing the computational time for a large number of grid blocks. Accordingly, the following formulation is used to obtain the nouniform grid spacing [49],

$$\Delta\xi_\nu = \frac{\chi^\nu}{\sum_{l=1}^{N_g}\chi^l}, \tag{41}$$

where $\Delta\xi$ is the grid spacing, N_g is the number of grid blocks, $\chi \geqslant 1$ is the mesh increment rate, and ν refers to the grid spacing index which starts from one for the first grid interval at the interface and ends with N_g for the last grid interval at the bottom or top of the domain. In order to obtain uniform grid spacing the value of χ in Eq. (41) should be equal to 1. However, in the present study, the mesh increment rate is chosen to be greater than 1, i.e., $1.005 \leqslant \chi \leqslant 1.01$. The grid convergence or mesh independence analysis is discussed in more detail in next subsection.

The numerical differentiation procedure that is used for unequal intervals is based on a three-point centered Lagrange polynomial approximation. Based on this approximation, the first and second spatial derivatives of a dependent variable f

with respect to ξ can be expressed as [50]

$$\frac{\partial f}{\partial \xi} = \frac{\Delta\xi^+}{\Delta\xi^+(\Delta\xi^- + \Delta\xi^+)} f_{j+1} - \frac{\Delta\xi^- - \Delta\xi^+}{\Delta\xi^-\Delta\xi^+} f_j - \frac{\Delta\xi^+}{\Delta\xi^-(\Delta\xi^- + \Delta\xi^+)} f_{j-1}, \quad (42)$$

$$\frac{\partial^2 f}{\partial \xi^2} = \frac{2}{\Delta\xi^+(\Delta\xi^- + \Delta\xi^+)} f_{j+1} - \frac{2}{\Delta\xi^+\Delta\xi^-} f_j + \frac{2}{\Delta\xi^-(\Delta\xi^- + \Delta\xi^+)} f_{j-1}, \quad (43)$$

where f is the perturbation eigenfunction in Eqs. (34)–(37), $\Delta\xi^+ = \xi_{j+1} - \xi_j$, $\Delta\xi^- = \xi_j - \xi_{j-1}$, and subscript j refers to the grid block index, which varies from 1 to $N_g + 1$. Discretizing Eqs. (34)–(37) based on Eqs. (42) and (43) results in an eigensystem, which can be compactly expressed as

$$\begin{bmatrix} A_1 - \sigma\mathbf{I} & B_1 \\ A_2 & B_2 - \sigma\mathbf{I} \end{bmatrix} \begin{bmatrix} \mathbf{S} \\ \mathbf{C} \end{bmatrix} = 0, \quad (44)$$

where $\mathbf{S}$ and $\mathbf{C}$ are the saturation and concentration eigenvectors, respectively; A_1, A_2, B_1, and B_1 are the discretization operators related to the eigenfunctions; and $\mathbf{I}$ is the identity matrix.

Note that the stream function equation Eq. (35) is eliminated by substituting it into the saturation and concentration perturbation equations [Eqs. (36) and (37)] and rearranging the resulting equations. Standard techniques are used to solve for the eigenvalues and eigenvectors [51], and only the largest eigenvalue is reported from the set of discrete eigenvalues. The results from the LSA are presented in the following subsection, which discusses the effect of the capillary transition zone on the growth of instability for a gravitationally unstable diffusive boundary layer.

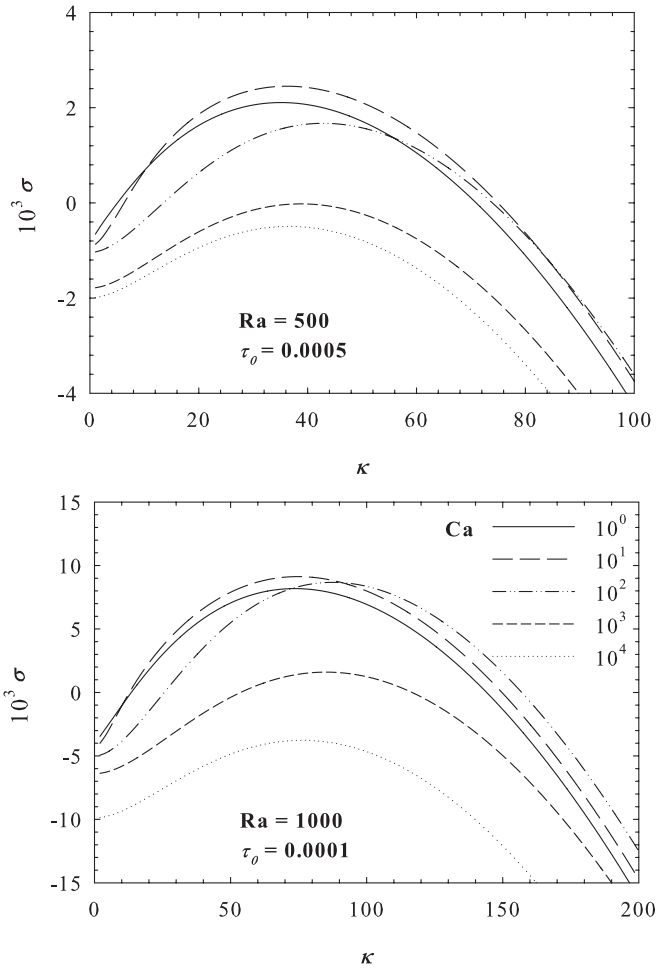

FIG. 3. Growth rate vs wave-number curves for Ra = 500 and 1000 for $\tau_0 = 0.0005$ and 0.0001, respectively, for different values of Ca. The other parameters are fixed: $n = 2$ and $\upsilon = 100$.

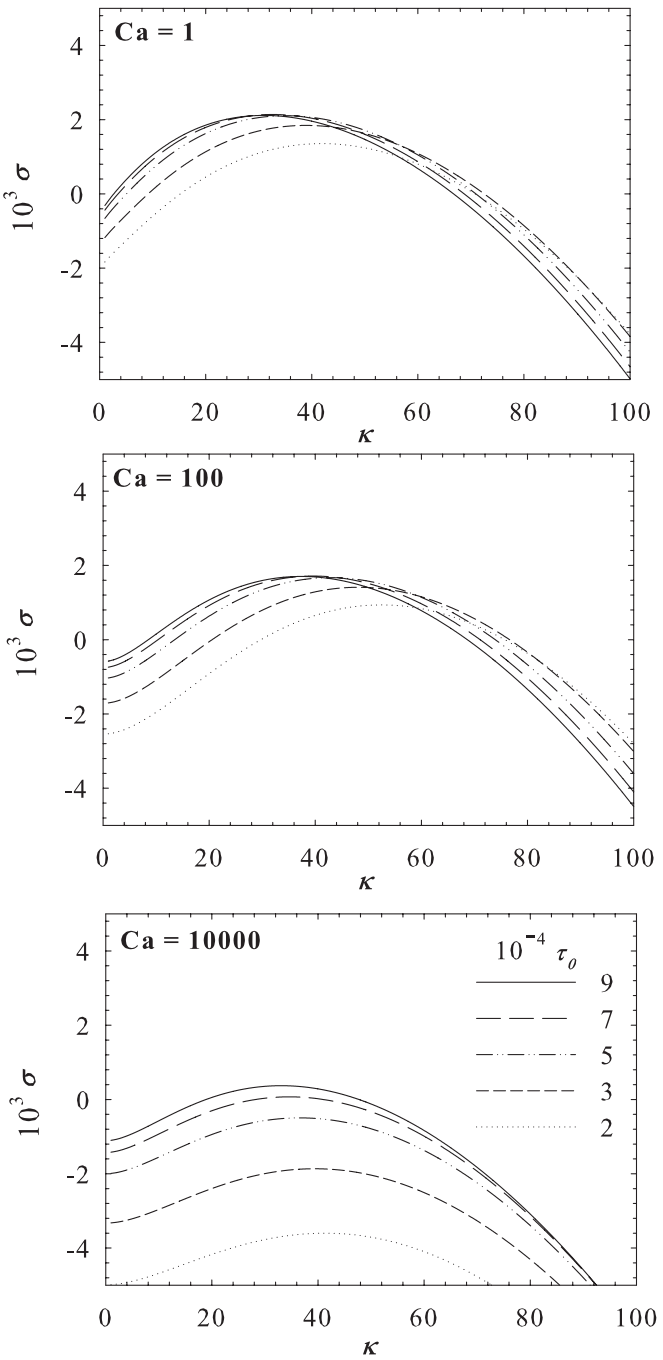

FIG. 4. Growth rate vs wave-number curves for Ca = 1, 10^2, and 10^4 at various τ_0. The other parameters are fixed: Ra = 500, $n = 2$, and $\upsilon = 100$.

C. LSA results

We first discuss the effect of the gravity number and viscosity ratio on the stability. Based on the schematic of the problem shown in Fig. 1, the displacement takes place in the z direction, and the denser fluid with the higher viscosity (wetting phase) is located under the lighter fluid with the lower viscosity (nonwetting phase). The stability of such a system can be examined with the following expression [52]:

$$\left(\frac{\mu_w}{k_{rw}} - \frac{\mu_n}{k_{rn}}\right)(V - V_c) \begin{cases} < 0 \Rightarrow \text{stable displacment} \\ > 0 \Rightarrow \text{unstable displacment} \end{cases}, \tag{45}$$

where $V_c = k\Delta\rho_{wn}g/(\mu_w/k_{rw} - \mu_n/k_{rn})$ and V is the base state advective velocity, which is equal to zero in our problem. This expression is always negative under the conditions of the problem. Therefore, the gravity number G and the mobility ratio M have no effect on the instability of the system, although they appeared in the stability analysis.

We now examine how the capillary number Ca combined with the Rayleigh number Ra affects the stability of the diffusive boundary layer. The growth rate versus the wave-number curves given by the QSSA are shown in Fig. 3 for different Ca at Ra = 500 and 1000 for τ_0 =0.0005 and 0.0001, respectively. The evolution of the maximum value of either the concentration or the saturation or the velocity (stream function) eigenfunction forms the basis of the growth rate plotted at τ_0 (a particular time) for each wave number. At an early time, the dynamical system is said to be stable if $\sigma < 0$ for every wave number, and a critical time τ_c (the onset of convection) is indicated when the growth rate just becomes positive at a critical wave number κ_c.

Figure 3 reveals that the flow system turns more stable as the capillary number increases. This can be expected and attributed to influence of the capillary height as it approaches zero ($h \to 0$) when Ca $\to \infty$. More precisely, at high Ca, the system behaves like a single-phase system (only the wetting phase), which behaves like an impervious boundary to flow at $\varsigma = 0$, i.e., the wetting phase has zero relative permeability at the interface. The capillary transition zone allows a crossflow at the interface and also acts as a feeding source, where the gas cap continuously feeds the underlying body of water. Therefore, convection is expected to begin faster in the presence of a capillary transition zone.

The results reveal that the growth of perturbation is not a monotonic function of Ca, which is due to distribution of the wetting phase in the transition zone, especially in the vicinity of the interface. This is analyzed in more detail in this subsection. Two physical processes are competing here: the diffusion of the gaseous component into the wetting phase, resulting in an unstable density profile, and the capillary force, which acts to increase the height of the transition zone. The zero or negative growth rates for small wave numbers (i.e., large wavelengths) implies that the system is always stable. Moreover, the critical wave number vanishes as the capillary number increases. Hence, for a given Ra and τ_0, the systems turns unstable at a critical wave number corresponding to a critical capillary number. Therefore, the onset time of convection for the two-phase system is characterized by the two dimensionless numbers of Ra and Ca.

Figure 4 describes the impact of the diffusion time on the stability of the boundary layer. The stability curves are plotted for three different capillary numbers, Ca = 1, 10^2, and 10^4. As shown, the system is more unstable for smaller capillary numbers. Note that, at lower values of Ra (e.g., 500), the capillarity

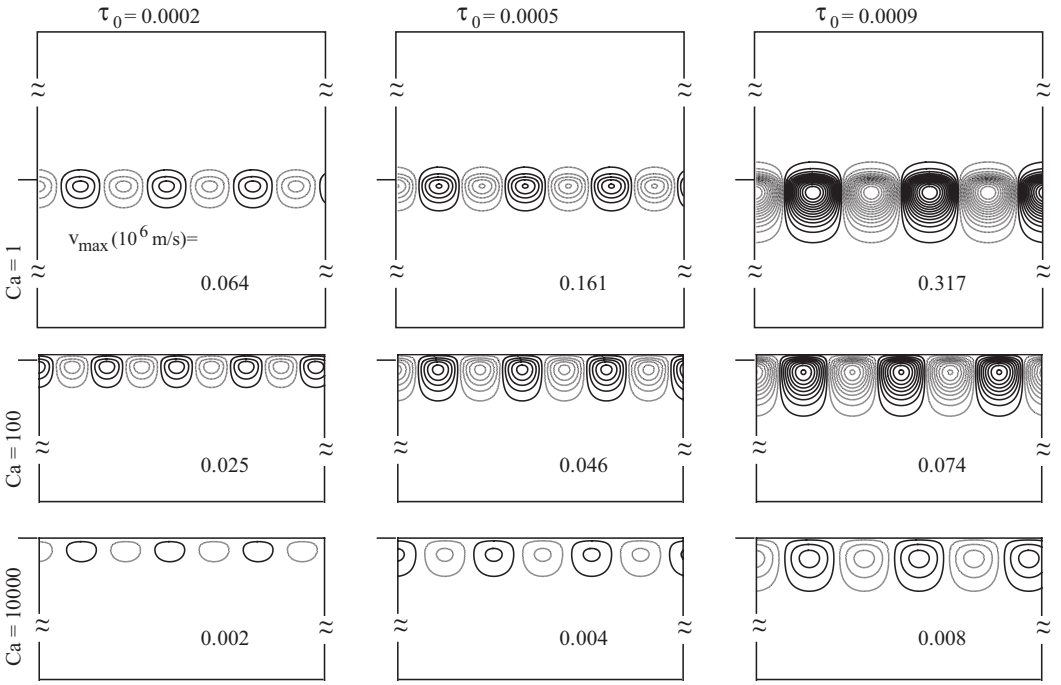

FIG. 5. Velocity contours at three different Ca and τ_0, where the numbers represent the maximum velocity of the fluid in μm/s. The other parameters are fixed: Ra = 500, $n = 2$, and $\upsilon = 100$.

is strong enough to compete with diffusion and convection. At a particular Ra, the most detrimental wave numbers and maximum growth rates are shifted to the larger values as τ_0 increases. Contrary to the small capillary numbers, the boundary layer becomes more stable as the front becomes more diffusive when capillary number increases, which means diffusion has a stabilizing effect on the system when the capillary effect is diminishing. Again, for a typical diffusion time, there may be a critical wave number when the convection evolves.

To comprehend the effect of a capillary transition zone on the stability of the diffusive boundary layer, the velocity contours for Ra = 500 for different values of capillary numbers related to Fig. 4 are presented in Fig. 5. The dimensional velocity fields are calculated by converting the perturbation stream functions back to the vertical and horizontal component of velocity using the following equations:

$$u_w = \sqrt{4\tau_0}\frac{D\varphi}{H}\sin(\kappa_{\max}\eta)e^{\sigma_{\max}\tau_0}\frac{\partial\Psi^*_{\max}}{\partial\xi}, \tag{46}$$

$$v_w = -\kappa_{\max}\frac{D\varphi}{H}\cos(\kappa_{\max}\eta)e^{\sigma_{\max}\tau_0}\Psi^*_{\max}, \tag{47}$$

where $\kappa_{\max}$ and $\sigma_{\max}$ are the wave number and the growth rate corresponding to the maximum perturbation stream function $\Psi^*_{\max}$, which itself corresponds to the largest eigenvalue obtained by solving Eq. (44).

For comparison purposes, the maximum value of velocity obtained from Eqs. (46) and (47) for each case is provided in Fig. 5. The comparison between the velocity contours at capillary numbers 1 and 10^4 reveals how the upward flow across the interface (crossflow) affects the onset of convection. Results shown in this figure reveal that, due to the small thickness of the transition zone, there is almost no crossflow at Ca = 10^4. On the other hand, at Ca = 1, the interaction between the diffusive boundary layer and the capillary transition zone increases the instability of the boundary layer such that the onset of instability occurs earlier, when the upward crossflow is accounted for. Furthermore, the number of convective cells increases as Ca decreases, which implies a smaller wavelength for the convection cells and confirms the stronger velocity field.

The critical time and its corresponding wave number for Ra values of 500, 1000, and 2000 are shown in Fig. 6. As expected, the flow becomes more unstable as Ra increases, due to the gravitationally unstable nature of the diffusive boundary layer. In fact, a larger density gradient across the boundary layer creates a more unstable front. As the capillary number decreases (Ca $\to$ 0), the boundary layer becomes more unstable, leading to larger wave numbers. This simply reflects the destabilizing effect of the capillary transition zone.

The variation of the capillary number in the range of Ca $\in [1, 10^4]$ shows a nonlinear dependence of τ_c and κ_c to the capillary number at a particular Ra. At large values of the capillary number (Ca $\to \infty$), the capillary transition zone has no significant effect on the stability of the diffusive boundary layer. Based on these observations, two regimes of instability can be identified; namely capillary-dominant and buoyancy-dominant regimes with a transition between them. In the capillary-dominant regime (Ca $\leqslant$ 1), capillarity plays the ultimate role in destabilizing the diffusive boundary layer; however, in the buoyancy-dominant regime (Ca $\geqslant 10^4$), the

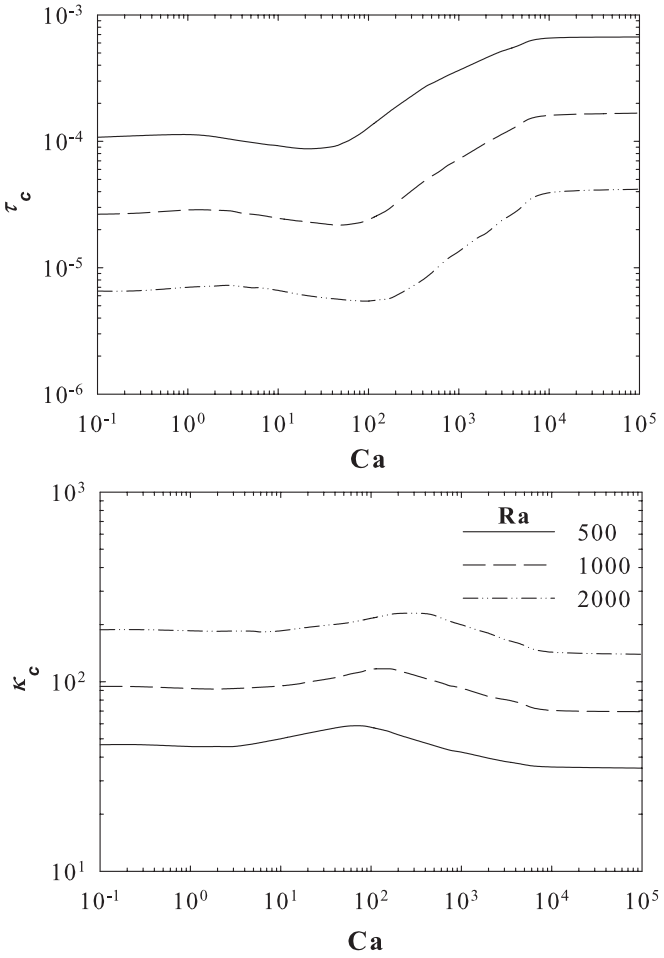

FIG. 6. Critical time and its corresponding wave-number curves for Ra = 500, 1000, and 2000 vs Ca, which shows the nonlinear dependence of τ_c and κ_c with Ca. The other parameters are fixed: $n = 2$ and $\upsilon = 100$.

capillary transition zone is small enough that it can be ignored, and the density difference $\Delta\rho_d^w$ (i.e., Ra) solely causes the instability of the diffusive boundary layer.

To better understand the dependency of τ_c and κ_c with Ca during the transition regime, the values of the wetting phase's relative permeability k_{rw} and $1/S_o(dS_o/d\varsigma)$ just above the interface must be analyzed. These two terms appear in the flow equation [Eq. (35)] and transport equation [Eq. (37)].

Figure 7 shows the behaviors of k_{rw} and $1/S_o(dS_o/d\varsigma)$ with regard to Ca at a point just above the interface. While the wetting phase relative permeability decreases, the latter term increases, suggesting that the relative permeability and the capillary diffusion are competing with each other. As the saturation of the wetting phase increases in the vicinity of the interface, the corresponding relative permeability also increases, which enhances the crossflow across the interface promoting instability of the diffusive boundary layer. In contrast, the abrupt changes in the saturation just above the interface results in larger values for $1/S_o(dS_o/d\varsigma)$, which strengthens the effect of diffusion in the transport equation, Eq. (37), and, consequently, delays flow instability. Figure 7 demonstrates that such a behavior is more pronounced for larger values of the material parameter at higher Ca.

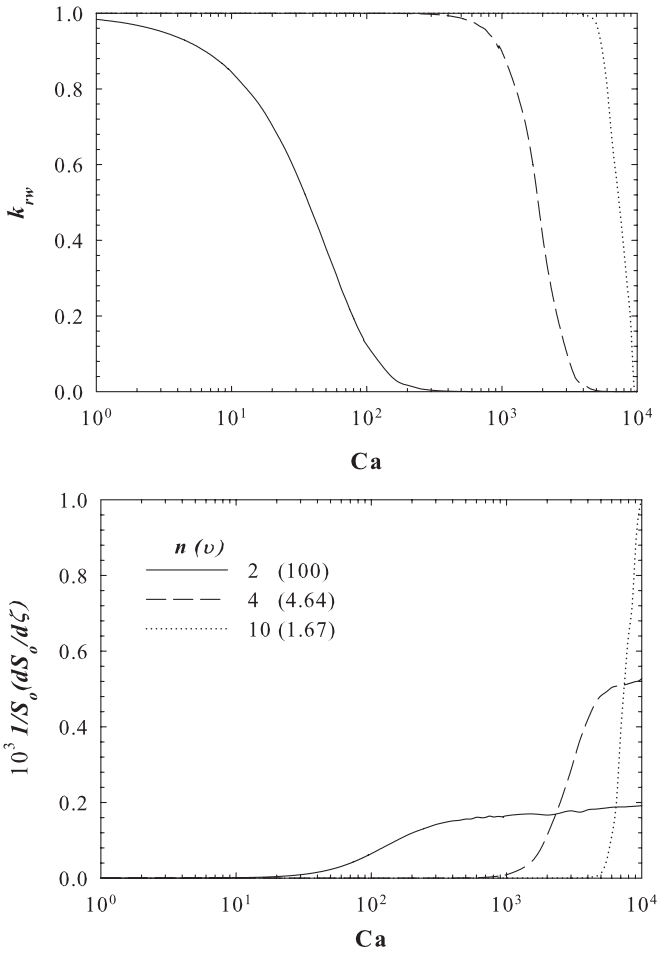

FIG. 7. Relative permeability of the wetting phase and $1/S_o(dS_o/d\varsigma)$ vs Ca at $n = 2$, 4, and 10. For a particular n, the value of υ is defined in such a way that the normalized wetting phase saturation S at top boundary tends to zero (i.e., $S = 0.001$).

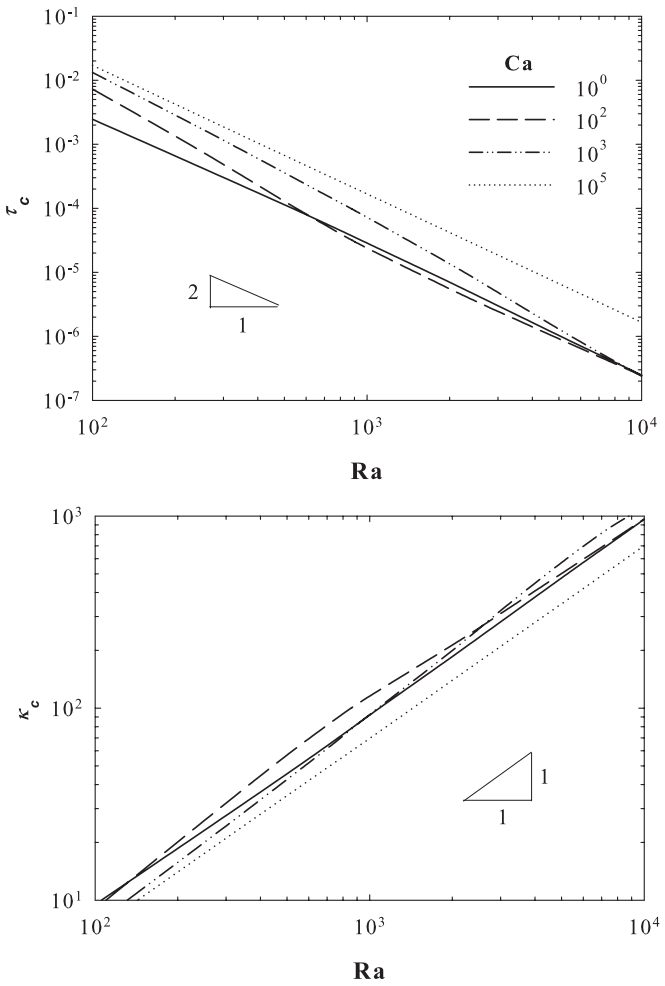

FIG. 8. Critical time and its corresponding wave-number curves vs Ra for different Ca. At very low and high values of Ca, the critical time varies with Ra^{-2}, while the critical wave number scales linearly with Ra. The other parameters are fixed: $n = 2$ and $\upsilon = 100$.

Further investigation is conducted by plotting the critical time and the critical wave number as a function of Ra at different capillary numbers. Figure 8 illustrates that, for both the lower (capillary-dominated regime, $\mathrm{Ca} \leqslant 1$) and upper (buoyancy-dominant regime, $\mathrm{Ca} \geqslant 10^4$) limits of the capillary number, the critical time varies with Ra^{-2}, while the critical wave number scales linearly with Ra. Similar scalings have been obtained by Caltagirone [32] but our analyses eliminate the effect of the boundary condition and consider the effect of the capillary transition zone, so the following scaling relations for the critical time and critical wave number are obtained:

$$\mathrm{Ca} \leqslant 1 \begin{cases} \tau_c \approx 25\ \mathrm{Ra}^{-2} \\ \kappa_c \approx 0.095\ \mathrm{Ra} \end{cases} \qquad \mathrm{Ca} \geqslant 10^4 \begin{cases} \tau_c \approx 162\ \mathrm{Ra}^{-2} \\ \kappa_c \approx 0.07\ \mathrm{Ra} \end{cases} . \tag{48}$$

These scaling relations show that the presence of the capillary transition zone can potentially decrease the onset time of convection by sixfold. Note that the above-mentioned scaling relationships apply only when $\sqrt{4\tau} \ll 1$ or the QSSA is deemed to be valid. The scaling relations obtained in present study in the absence of a capillary transition zone ($\mathrm{Ca} \geqslant 10^4$), Eq. (48), are in close agreement with the critical time to onset of convection and the critical wave number found by Kim and Choi [28]. Although, the onset of convection in the absence of a capillary transition zone has been studied extensively, the effect of capillarity on the onset of natural convection has not been studied in the past.

Further examination is carried out to analyze the impact of Ra on the stability of the boundary layer by studying the onset of instability. Figure 9 depicts the velocity contours for two different cases: one for a small $\mathrm{Ca} = 1$, representing the capillary-dominant regime, and the other for a large $\mathrm{Ca} = 10^4$, representing the buoyancy-dominant regime. In the comparison of these two cases, one may observe that the flow system is more stable in the buoyancy-dominant regime ($\mathrm{Ca} \geqslant 10^4$).

Velocity contours at different Ra in Fig. 9 demonstrate that the wavelengths decrease with increasing Ra, resulting in the evolution of a stronger convection current earlier in the mixing process. Results also show that, in the case of capillary-dominant flow, the convective currents penetrate upward into the capillary transition zone and most likely improve the mixing process. Such an observation has not been made for the buoyancy-dominant flow regime.

The maximum growth rate $\sigma_{\max}$ as a function of time and the corresponding most detrimental mode $\kappa_{\max}$ for the low and high limits of capillary numbers at different Rayleigh numbers

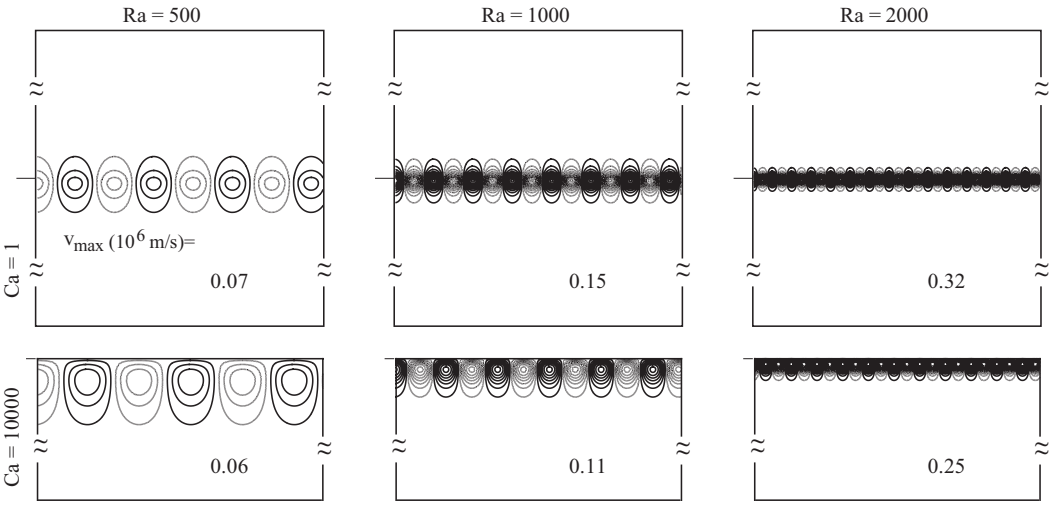

FIG. 9. Velocity contours at Ca = 1 and 10^4 for three different Ra at the onset of instability, where the numbers represent the maximum velocity of the fluid in μm/s. The other parameters are fixed: $n = 2$ and $\upsilon = 100$.

are depicted in Fig. 10. These results show that, after the onset of convection, the maximum growth rate σ_{max} rapidly reaches a maximum value. In the later time of the evolution, σ_{max} decays slowly and is scaled with $\tau^{2/5}$. The most detrimental wave number displays $\tau^{1/4}$ scaling, which is similar to the result obtained by Riaz *et al.* [30]. These observations clearly

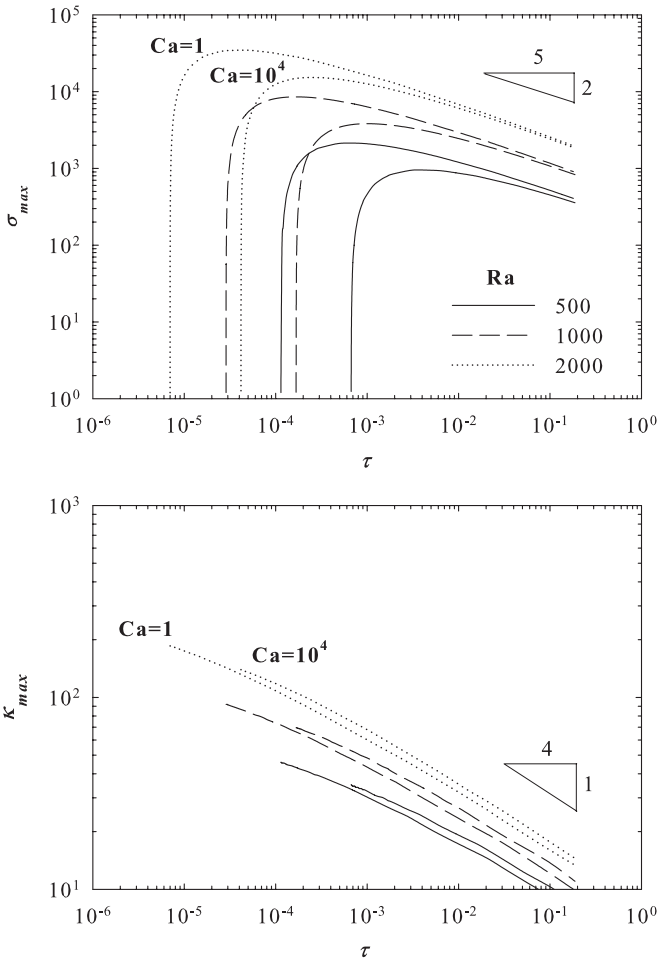

FIG. 10. Maximum growth rate and the most detrimental wave number as a function of time for Ra = 500, 1000, and 2000 at the lower and higher limits of Ca. The other parameters are fixed: $n = 2$ and $\upsilon = 100$.

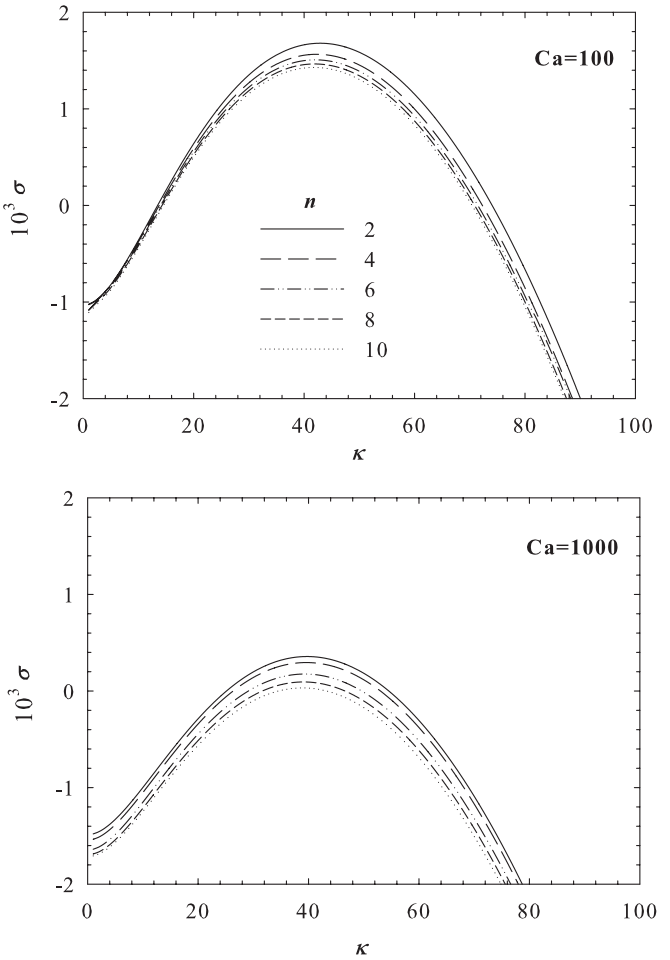

FIG. 11. Growth rate vs wave-number curves for Ca = 100 and Ca = 1000 for different values of material parameters n. The other parameters are fixed: Ra = 500 and $\tau_0 = 0.0005$.

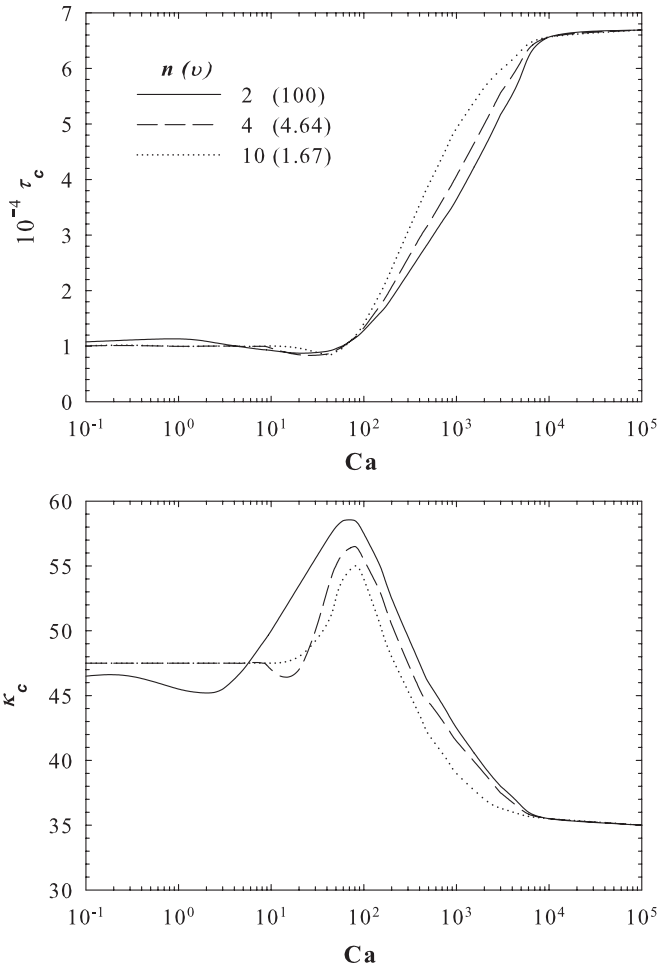

FIG. 12. Critical time and its corresponding wave-number curves vs Ca for different values of n. The other parameters are fixed: Ra = 500 and $\tau_0 = 0.0005$.

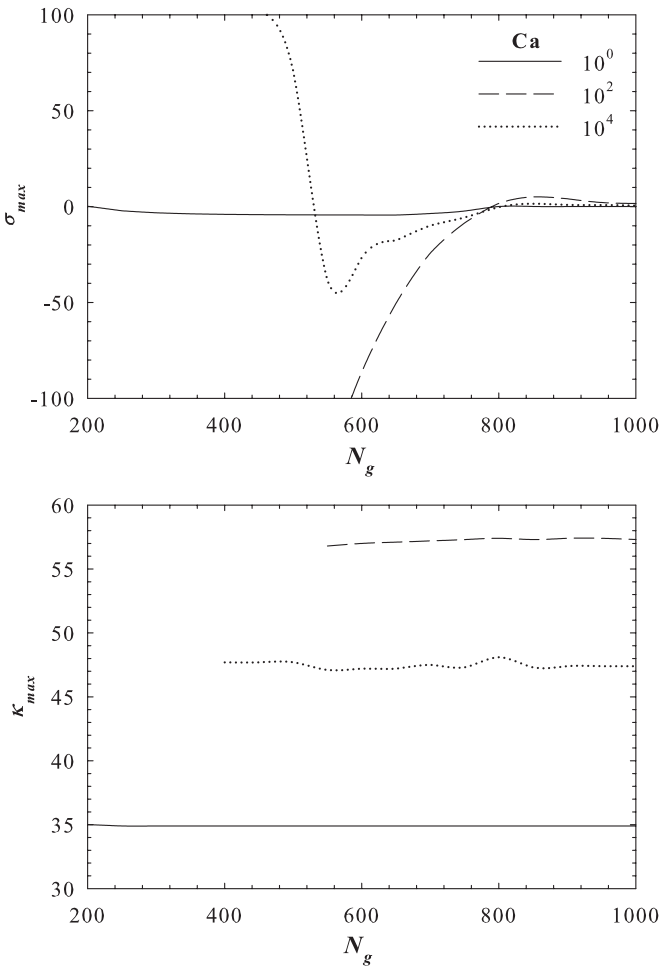

FIG. 13. Maximum growth rate and the most detrimental wave number as a function of the number of grids for Ca = 1, 10^2, and 10^4. The other parameters are fixed: Ra = 500, $n = 2$, and $\upsilon = 100$.

describe that the flow system becomes less unstable as the diffusion increases around the boundary layer.

In order to find the effect of the material parameter on the onset of instability, the growth rate versus wave-number curves for different n at Ca = 100 and 1000 are given in Fig. 11. This figure reveals that the flow system becomes more unstable as n increases. This can be attributed to the larger amount of wetting phase saturation, S just above the interface, which manifests itself in k_{rw}. From a quick comparison between the instability curves for Ca = 100 and 1000, one may notice that the effect of n is more evident at Ca = 1000, although the onset occurs earlier at Ca = 100.

For a better understanding of the mutual effect of n and Ca on the onset time, the critical times and their associated wave-number curves for different n versus Ca are given in Fig. 12. This figure reveals that the material parameter has no significant influence on the onset of instability in both capillary- and buoyancy-dominant regimes. It can be observed that the onset time and the critical wave number are considerably responsive to the material parameter in the transition regime.

Before comparing the LSA results with the results obtained from nonlinear simulations, we examine accuracy of the algorithm developed to solve Eq. (44) by showing mesh independence of the leading eigenvalue and most unstable wave number. The maximum growth rate $\sigma_{\max}$ as a function of number of grid blocks N_g and the corresponding most detrimental mode $\kappa_{\max}$ for Ca = 1, 100, and 10 000 at Ra = 500 are depicted in Fig. 13. This figure shows how the algorithm copes with change in grid spacing and how very close it is in having grid independence at $N_g \geqslant 800$. As can be seen, the maximum growth rate $\sigma_{\max}$ changes as the number of grids increases and at $N_g \geqslant 800$ it stabilizes around a positive value slightly greater than zero (the onset of convection). In contrast, the most detrimental wave number corresponds only slightly with respect to the number of grids or the grid spacing.

IV. NONLINEAR SIMULATIONS

A. Numerical approach

Nonlinear mixing dynamics in the presence of a capillary force are investigated by solving the nonlinear problem using highly refined direct numerical simulations. In order to examine the nonlinear development of mixing, Eqs. (1)–(8) are solved numerically. The 2D numerical solution developed in this work evaluates convective mixing considering the effect of the capillary transition zone. The model is based on solving,

first, for the pressure field and then for the saturation and composition. In other words, the implicit pressure and explicit mole fractions and saturations (IMPECS) are employed. Such formulations can perform well in large-scale flow simulation where the numerical stability limitations are not severe [40]. For modeling a highly nonlinear convective flow, the explicit methods that are conditionally stable, but of higher accuracy, are prone to generating nonphysical perturbations, unless the grid block size and time step are sufficiently small. To control the oscillations due to temporal and spatial discretizations, the grid Courant, Peclet, and Rayleigh numbers are checked to meet the specific criteria and to assure the numerical accuracy [17].

The numerical model is based on the formulation for multicomponent and multiphase flow presented by Aziz and Settari [40]. A two-component and two-phase model is employed. In this model, the nonwetting phase is present in both phases, while the wetting phase is present only in the aqueous phase. Detailed information of the fluid properties employed in fluid model is presented by Hassanzadeh *et al*. [53].

The governing equations are discretized based on a finite difference formulation in a block-centered Cartesian grid system, where the grid blocks can be uniform or nonuniform. As mentioned before, the pressure equation is discretized implicitly in pressure, while the transmissibilities are approximated explicitly. The Picard iteration is incorporated to alleviate the nonlinearity and solve the pressure and component balance equation. The calculated pressure distribution is then used to obtain the velocity field. The pressure and velocity fields are used in component mass balance equations to obtain the mass of each component for all grid blocks at each time step. Eventually, the calculated parameters are used to perform a new iteration, and the calculations are repeated until convergence is achieved.

B. Direct numerical simulation results

Direct numerical simulations are presented here to discuss the nonlinear dynamics of fingering by analyzing the temporal and spatial concentration distributions for Ra = 500. To see how a capillary transition zone may affect the stability of the boundary layer, the concentration contours are plotted for the capillary-dominant, transition, and buoyancy-dominant regimes.

Figure 14 depicts the concentration contours at different times. These three simulations are carried out with the number of grids at 200×100 and where the height of the system above and below the gas-water contact is considered to be

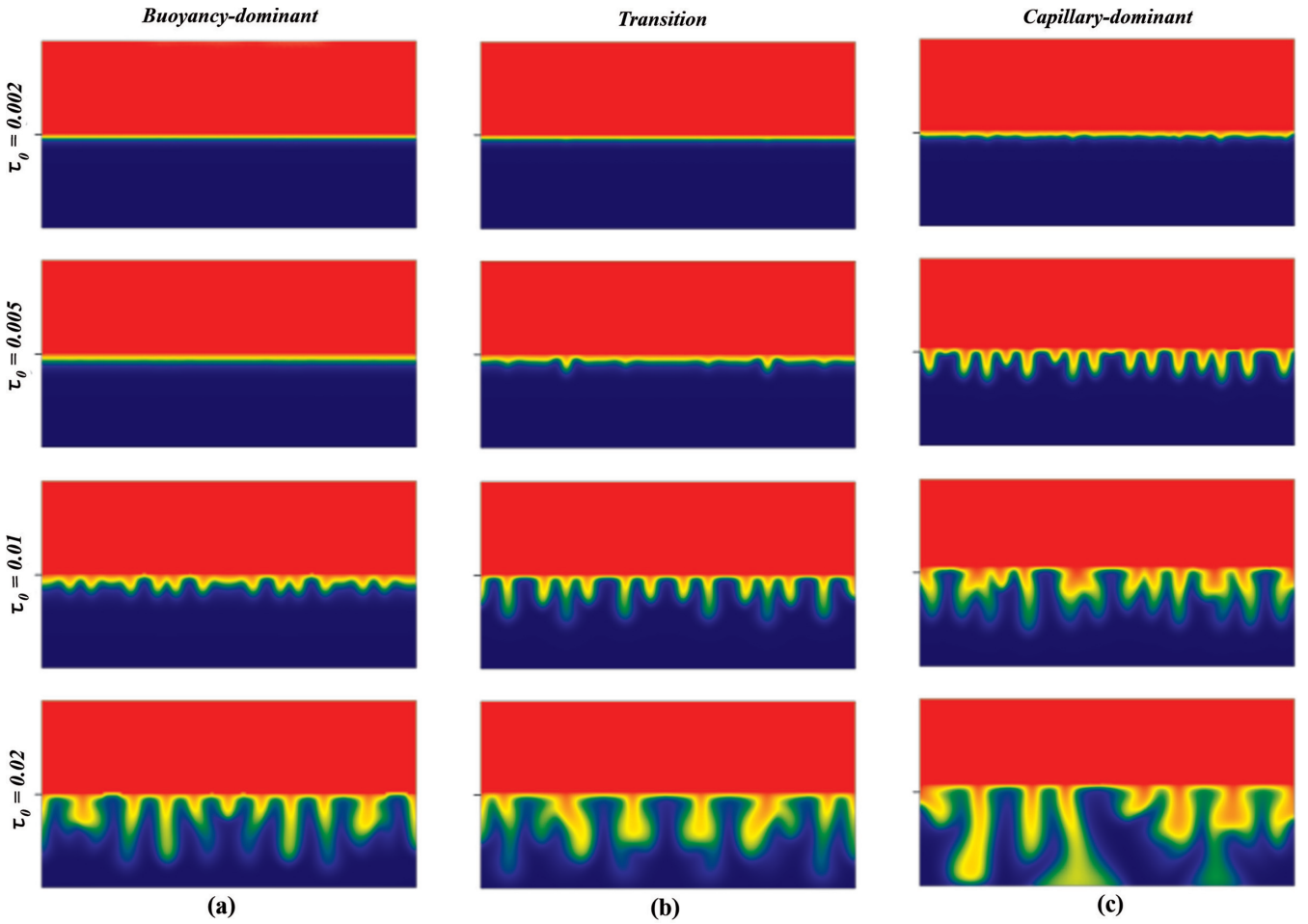

FIG. 14. (Color online) Concentration contours at different times for Ra = 500, where top of the domain shows $C = 1$ [red (light gray)] and bottom of the domain shows $C = 0$ [blue (dark gray)], respectively, representing (a) the buoyancy-dominant regime, (b) the transition regime, and (c) the capillary-dominant regime.

the same. However, the capillary transition zone differs for each case, representing different regimes. The same relative permeabilities and capillary pressure constitutive relations given in the stability analysis section [Eqs. (24)–(26)] are employed with $n = 2$. It can be observed that the flow is destabilized, as predicted by the present stability analysis, and fingers of high-density fluid start to grow with time (Fig. 5). The boundary layer is initially stable, but the fingering phenomenon appears as time passes. The fingers gradually grow and interact with each other at later times, until they reach the bottom boundary, which is closed. Consequently, the concentration of the diffusive component c_d^w builds in the wetting phase region and becomes saturated with respect to the dissolving component.

Figure 14 illustrates the concentration contours for $h \sim 0$, $h \sim H/5$, and $h \sim H$, representing the buoyancy-dominant, transition, and capillary-dominant regimes, respectively. As predicted by the linear stability analysis, the larger h results in faster development of the instability. Furthermore, the fingering pattern is dramatically changed as h is increased. The change is very great, such that the convective mixing is delayed significantly in the absence of the capillary transition zone for the buoyancy-dominant case ($h \sim 0$). The front convects faster in the capillary-dominant regime ($h \sim H$) compared with the buoyancy-dominant regimes. This confirms the predictions from the linear stability analysis.

V. CONCLUSIONS

This study presents a macroscopic transport model of the buoyancy-driven convective flow in a saturated porous medium in the presence of a capillary transition zone. The gravitational stability of the diffusive boundary layer underneath a capillary transition zone was studied using the QSSA. The results of the LSA reveal that the capillary transition zone destabilizes the diffusive boundary layer, due to the flow across the interface. Furthermore, the instability problem is characterized by capillary-dominant ($\mathrm{Ca} \leqslant 1$) and buoyancy-dominant ($\mathrm{Ca} \geqslant 10^4$) regimes with a transition ($1 < \mathrm{Ca} < 10^4$) regime in between. The results presented in this study provide a new understanding of the effects of a capillary transition zone on the instability of the diffusive boundary layer.

The scaling relations for the most unstable growth rate and wave number and the critical time and its corresponding wave number, which were obtained by the LSA, are in quantitative agreement with the scaling relations reported in the literature. In the capillary-dominant regime, the capillarity has a strong role in destabilizing the diffusive boundary layer, where the critical time scales as $\tau_c \approx 25\ \mathrm{Ra}^{-2}$. On the other hand, in case of the buoyancy-dominant regime, where the capillary transition zone is negligible, the critical time scales as $\tau_c \approx 162\ \mathrm{Ra}^{-2}$. Furthermore, for long times, the maximum growth rate decays slowly as $\tau^{2/5}$, while the most detrimental wave number scales as $\tau^{1/4}$ for the both instability regimes.

Direct numerical simulations were also conducted to observe the development of instability of the diffusive boundary layer for different regimes identified in the LSA. It was revealed that a larger capillary transition zone results in faster development of instability, as predicted by the LSA. Moreover, the capillary transition zone significantly affects the fingering pattern such that the natural convection occurs considerably faster for the capillary-dominant regime than for the buoyancy-dominant regime.

ACKNOWLEDGMENTS

This research was enabled with financial support from the Natural Sciences and Engineering Research Council of Canada (NSERC) and the Department of Chemical and Petroleum Engineering at the University of Calgary and with the use of computing resources provided by WestGrid and Compute Canada.

[1] D. A. Nield and A. Bejan, *Convection in Porous Media* (Springer Verlag, Berlin, 2006).
[2] V. Frette, J. Feder, T. Jøssang, and P. Meakin, Phys. Rev. Lett. **68**, 3164 (1992).
[3] R. L. Van Dam, C. T. Simmons, D. W. Hyndman, and W. W. Wood, Geophys. Res. Lett. **36**, L11403 (2009).
[4] J. J. Hidalgo, J. Fe, L. Cueto-Felgueroso, and R. Juanes, Phys. Rev. Lett. **109**, 264503 (2012).
[5] J. T. H. Andres and S. S. S. Cardoso, Chaos **22**, 037113 (2012).
[6] C. Horton and F. Rogers, J. Appl. Phys. **16**, 367 (1945).
[7] E. R. Lapwood, Math. Proc. Cambridge Philos. Soc. **44**, 508 (1948).
[8] H. J. G. Diersch and O. Kolditz, Adv. Water Res. **25**, 899 (2002).
[9] P. Vadasz, *Emerging Topics in Heat and Mass Transfer in Porous Media* (Springer, Dordrecht, Netherlands, 2008), Vol. 22, p. 85.
[10] P. Cheng, Advances in Heat Transfer **14**, 1 (1978).
[11] M. Kaviany, *Principles of Convective Heat Transfer* (Springer Verlag, Berlin, 2001).
[12] A. J. Smith, Water Resour. Res. **40**, W08309 (2004).
[13] J. A. Neufeld, M. A. Hesse, A. Riaz, M. A. Hallworth, H. A. Tchelepi, and H. E. Huppert, Geophys. Res. Lett. **37**, L22404 (2010).
[14] J. T. H. Andres and S. S. S. Cardoso, Phys. Rev. E **83**, 046312 (2011).
[15] P. A. Tsai, K. Riesing, and H. A. Stone, Phys. Rev. E **87**, 011003 (2013).
[16] H. Emami Meybodi and H. Hassanzadeh, Water Resour. Res. **47**, W12504 (2011).
[17] H. Emami Meybodi and H. Hassanzadeh, AlChE J., doi: 10.1002/aic.13891 (2012).
[18] M. T. Elenius, J. M. Nordbotten, and H. Kalisch, IMA J. Appl. Math. **77**, 771 (2012).
[19] B. Morton, Q. J. Mech. Appl. Math. **10**, 433 (1957).
[20] M. Kaviany, Int. J. Heat Mass Transf. **27**, 2101 (1984).
[21] M. C. Kim and S. Kim, Int. Commun. Heat Mass Transfer **32**, 416 (2005).
[22] W. Lick, J. Fluid Mech. **21**, 565 (1965).
[23] T. D. Foster, Phys. Fluids **8**, 1249 (1965).

[24] T. D. Foster, Phys. Fluids **11**, 1257 (1968).
[25] J. Ennis-King, I. Preston, and L. Paterson, Phys. Fluids **17**, 084107 (2005).
[26] L. Cueto-Felgueroso and R. Juanes, Phys. Rev. E **79**, 036301 (2009).
[27] S. Backhaus, K. Turitsyn, and R. E. Ecke, Phys. Rev. Lett. **106**, 104501 (2011).
[28] M. C. Kim and C. K. Choi, Phys. Fluids **24**, 044102 (2012).
[29] A. C. Slim and T. Ramakrishnan, Phys. Fluids **22**, 124103 (2010).
[30] A. Riaz, M. Hesse, H. Tchelepi, and F. Orr, J. Fluid Mech. **548**, 87 (2006).
[31] A. Selim and D. A. S. Rees, J. Porous Media **10**, 1 (2007).
[32] J. P. Caltagirone, Q. J. Mech. Appl. Math. **33**, 47 (1980).
[33] X. Xu, S. Chen, and D. Zhang, Adv. Water Res. **29**, 397 (2006).
[34] H. Hassanzadeh, M. Pooladi-Darvish, and D. W. Keith, Transp. Porous Media **65**, 193 (2006).
[35] K. K. Tan, T. Sam, and H. Jamaludin, Int. J. Heat Mass Transf. **46**, 2857 (2003).
[36] G. Homsy, J. Fluid Mech. **60**, 129 (1973).
[37] D. Y. Yoon and C. K. Choi, Korean J. Chem. Eng. **6**, 144 (1989).
[38] K. Ghesmat, H. Hassanzadeh, and J. Abedi, J. Fluid Mech. **673**, 480 (2011).
[39] J. Robinson, Phys. Fluids **19**, 778 (1976).
[40] K. Aziz and A. Settari, *Petroleum Reservoir Simulation* (Applied Science Publishers London, 1979).
[41] J. Bear, *Dynamics of Fluids in Porous Media* (Dover, London, 1988).
[42] M. C. Leverett, Trans. Am. Inst. Min., Metall. Pet. Eng. **142**, 152 (1941).
[43] P. G. De Gennes, Rev. Mod. Phys. **57**, 827 (1985).
[44] M. T. Van Genuchten, Soil Sci. Soc. Am. J. **44**, 892 (1980).
[45] Y. Mualem, Water Resour. Res. **12**, 1248 (1976).
[46] A. T. Corey, *Mechanics of Immiscible Fluids in Porous Media* (Water Resources Publication, Colorado, 1994).
[47] M. N. Ozisik, *Heat Conduction* (John Wiley & Sons, New York, 1993).
[48] C. Tan and G. Homsy, Phys. Fluids **29**, 3549 (1986).
[49] J. D. Hoffman, *Numerical Methods for Engineers and Scientists* (CRC Press, New York, 2001).
[50] A. K. Singh and B. Bhadauria, Int. J. Math. Anal. **3**, 815 (2009).
[51] A. Riaz and H. A. Tchelepi, Phys. Fluids **16**, 4727 (2004).
[52] C. Marle, *Multiphase Flow in Porous Media* (Éditions technip, Paris, 1981).
[53] H. Hassanzadeh, M. Pooladi-Darvish, A. M. Elsharkawy, D. W. Keith, and Y. Leonenko, Int. J. Greenhouse Gas Control **2**, 65 (2008).